Monthly Notices of the ROYAL ASTRONOMICAL SOCIETY **MNRAS Advance Access published September 12, 2013**

MNRAS (2013) doi:10.1093/mnras/stt1535

The Atacama Cosmology Telescope: the stellar content of galaxy clusters selected using the Sunyaev–Zel'dovich effect

Matt Hilton,[1,2]★ Matthew Hasselfield,[3] Cristóbal Sifón,[4] Andrew J. Baker,[5] L. Felipe Barrientos,[6] Nicholas Battaglia,[7,8] J. Richard Bond,[8] Devin Crichton,[9] Sudeep Das,[10,11] Mark J. Devlin,[12] Megan Gralla,[9] Amir Hajian,[8] Adam D. Hincks,[8] John P. Hughes,[5] Leopoldo Infante,[6] Kent D. Irwin,[13] Arthur Kosowsky,[14] Yen-Ting Lin,[15] Tobias A. Marriage,[9] Danica Marsden,[16] Felipe Menanteau,[5] Kavilan Moodley,[2] Michael D. Niemack,[17] Mike R. Nolta,[8] Lyman A. Page,[18] Erik D. Reese,[12] Jon Sievers,[8,18] David N. Spergel[19] and Edward J. Wollack[20]

[1]*Centre for Astronomy & Particle Theory, School of Physics and Astronomy, University of Nottingham NG7 2RD, UK*
[2]*Astrophysics & Cosmology Research Unit, School of Mathematics, Statistics & Computer Science, University of KwaZulu-Natal, Durban 4041, South Africa*
[3]*Department of Physics and Astronomy, University of British Columbia, Vancouver, BC V6T 1Z4, Canada*
[4]*Leiden Observatory, Leiden University, PO Box 9513, NL-2300 RA Leiden, the Netherlands*
[5]*Department of Physics and Astronomy, Rutgers, The State University of New Jersey, 136 Frelinghuysen Road, Piscataway, NJ 08854-8019, USA*
[6]*Departamento de Astronomía y Astrofísica, Facultad de Física, Pontificía Universidad Católica, Casilla 306, Santiago 22, Chile*
[7]*Department of Physics, Carnegie Mellon University, Pittsburgh, PA 15213, USA*
[8]*Canadian Institute for Theoretical Astrophysics, University of Toronto, Toronto, ON M5S 3H8, Canada*
[9]*Department of Physics and Astronomy, The Johns Hopkins University, 3400 N. Charles St., Baltimore, MD 21218-2686, USA*
[10]*Argonne National Laboratory, 9700 S. Cass Avenue, Lemont, IL 60439, USA*
[11]*Berkeley Center for Cosmological Physics, LBL and Department of Physics, University of California, Berkeley, CA 94720, USA*
[12]*Department of Physics and Astronomy, University of Pennsylvania, 209 South 33rd Street, Philadelphia, PA 19104, USA*
[13]*NIST Quantum Devices Group, 325 Broadway Mailcode 817.03, Boulder, CO 80305, USA*
[14]*Department of Physics and Astronomy, University of Pittsburgh, Pittsburgh, PA 15260, USA*
[15]*Institute of Astronomy and Astrophysics, Academia Sinica, Taipei, Taiwan*
[16]*Department of Physics, University of California Santa Barbara, CA 93106, USA*
[17]*Department of Physics, Cornell University, Ithaca, NY 14853, USA*
[18]*Joseph Henry Laboratories of Physics, Jadwin Hall, Princeton University, Princeton, NJ 08544, USA*
[19]*Department of Astrophysical Sciences, Peyton Hall, Princeton University, Princeton, NJ 08544, USA*
[20]*NASA/Goddard Space Flight Center, Greenbelt, MD 20771, USA*

Accepted 2013 August 14. Received 2013 August 9; in original form 2013 January 4

ABSTRACT

We present a first measurement of the stellar mass component of galaxy clusters selected via the Sunyaev–Zel'dovich (SZ) effect, using 3.6 and 4.5 μm photometry from the *Spitzer Space Telescope*. Our sample consists of 14 clusters detected by the Atacama Cosmology Telescope (ACT), which span the redshift range $0.27 < z < 1.07$ (median $z = 0.50$) and have dynamical mass measurements, accurate to about 30 per cent, with median $M_{500} = 6.9 \times 10^{14}$ M$_\odot$. We measure the 3.6 and 4.5 μm galaxy luminosity functions, finding the characteristic magnitude (m^*) and faint-end slope (α) to be similar to those for infrared-selected cluster samples. We perform the first measurements of the scaling of SZ observables (Y_{500} and y_0) with both brightest cluster galaxy (BCG) stellar mass and total cluster stellar mass ($M_{500}^{\rm star}$). We find a significant correlation between BCG stellar mass and Y_{500} ($E(z)^{-2/3}\, D_A^2\, Y_{500} \propto M_*^{1.2\pm0.6}$), although we are not able to obtain a strong constraint on the slope of the relation due to the small sample size. Additionally, we obtain $E(z)^{-2/3}\, D_A^2\, Y_{500} \propto M_{500}^{\rm star\ 1.0\pm0.6}$ for the scaling with total stellar mass. The mass fraction in stars spans the range 0.006–0.034, with the second

★ E-mail: hiltonm@ukzn.ac.za

ranked cluster in terms of dynamical mass (ACT-CL J0237−4939) having an unusually low total stellar mass and the lowest stellar mass fraction. For the five clusters with gas mass measurements available in the literature, we see no evidence for a shortfall of baryons relative to the cosmic mean value.

Key words: galaxies: clusters: general – galaxies: luminosity function, mass function – galaxies: stellar content – cosmology: observations.

1 INTRODUCTION

Galaxy clusters are the most massive gravitationally bound objects in the Universe, and as such their changing abundance with redshift traces the process of structure formation. By studying the evolution of their properties with redshift, we can learn the assembly history of their constituent dark matter, gas and galaxies. The large masses of clusters ensure that the gas and stellar mass observed within them remain gravitationally bound. They therefore represent a fair sample of the Universe as it evolves over cosmic time. Measurements of cluster gas fractions have been used to constrain cosmological parameters, including the dark energy equation of state (e.g. Allen et al. 2008). While the hot gas in clusters makes up the majority of the baryonic component (around 80 per cent), accurate measurements of the mass fraction in the minority stellar component are also required to gain insight into the physical processes occurring within clusters.

It is known that the physics which determines the properties of the intracluster medium (ICM) is more complicated than simply the action of gravitational collapse alone, as the observed scaling relations, such as between X-ray luminosity and temperature, deviate from the self-similar expectation (e.g. Markevitch 1998; Arnaud & Evrard 1999; Pratt et al. 2009), indicating that an additional source of energy is heating the ICM. While some energy is injected by supernovae (SNe) within galaxies, it is likely that the bulk of the energy comes from active galactic nuclei (AGN) in the centres of clusters, as observations of low-redshift clusters show that AGN jets, seen in radio imaging, carve out cavities in the hot gas observed at X-ray wavelengths (e.g. Bîrzan et al. 2004; McNamara et al. 2005; Blanton et al. 2011). Feedback by AGN and SNe must also leave an imprint on the galaxy populations of clusters, and is a crucial component of galaxy formation models (e.g. Bower et al. 2006; De Lucia et al. 2006; Bower, McCarthy & Benson 2008), where it is invoked to quench star formation in massive haloes. Therefore, in principle, it is possible to constrain the strength of feedback processes by measuring the stellar fractions of clusters (e.g. Bode, Ostriker & Vikhlinin 2009).

The baryon fractions of clusters in the local Universe have been measured by several studies (e.g. Lin, Mohr & Stanford 2003; Gonzalez, Zaritsky & Zabludoff 2007; Andreon 2010; Balogh et al. 2011). They find that the mass fraction contained in stars is smaller for more massive clusters, while conversely the gas fractions are larger (e.g. Gonzalez et al. 2007). Within R_{500} (the radius at which the enclosed density is 500 times the critical density of the Universe), there may be a shortfall of baryons with respect to the cosmic value inferred from measurements of the cosmic microwave background ($f_{\rm b} = 0.166 \pm 0.020$; Komatsu et al. 2011), with cluster studies finding $f_{\rm b} \approx 0.13$ (e.g. Gonzalez et al. 2007), although the uncertainties are large and subject to various systematic effects. There are few measurements at intermediate redshift: Giodini et al. (2009) describe measurements of the baryon fractions in $0.1 < z < 1$ groups and clusters found in the COSMOS (Scoville et al. 2007) field, while Lin et al. (2012) present estimates for a heterogeneous sample of 45 clusters at $0.1 < z < 0.6$ using archival X-ray data and infrared (IR) photometry from the *Wide-Field Infrared Survey Explorer* (*WISE*; Wright et al. 2010).

In this paper, we report a first characterization of the stellar fractions, stellar mass scaling relations and properties of brightest cluster galaxies (BCGs), using IR data from the *Spitzer Space Telescope*, for a sample of galaxy clusters selected via the Sunyaev–Zel'dovich effect (SZ; Sunyaev & Zeldovich 1972) by the Atacama Cosmology Telescope (ACT; Swetz et al. 2011). The SZ effect is the inverse Compton scattering of cosmic microwave background photons by electrons in the hot gas atmospheres of clusters. In principle, it allows the construction of approximately mass-limited, redshift-independent samples of clusters (see e.g. the review by Carlstrom, Holder & Reese 2002).

The structure of this paper is as follows. In Section 2, we briefly describe the cluster sample and associated ancillary data, which include dynamical mass estimates obtained from extensive spectroscopic observations with 8-m class telescopes (Sifón et al. 2012). We also describe the processing of the *Spitzer* IR imaging used in this work. In Section 3, we present a measurement of the 3.6 and 4.5 μm galaxy luminosity functions (LFs), and compare our findings with results obtained for IR-selected cluster samples. We examine the IR properties of the BCGs, and their scaling relations with dynamical mass and SZ observables in Section 4. We similarly present scaling relations with total stellar mass and the stellar fractions in Section 5. We discuss our findings in Section 6 and conclude in Section 7.

We assume a cosmology with $\Omega_{\rm m} = 0.3$, $\Omega_\Lambda = 0.7$ and $H_0 = 70$ km s^{-1} Mpc^{-1} throughout the paper. All magnitudes are on the AB system (Oke 1974), unless otherwise stated. We adopt a Salpeter (1955) initial mass function (IMF) for stellar mass estimates. All estimates of cluster masses and SZ signals are measured within a characteristic radius defined with respect to the critical density at the cluster redshift.

2 DATA AND OBSERVATIONS

2.1 Cluster sample and optical observations

The cluster sample used in this work is drawn from the Marriage et al. (2011) SZ-selected cluster catalogue, detected in 148 GHz observations (conducted in 2008) with ACT, a 6-m telescope located in Northern Chile. The pipeline used to produce maps (directly calibrated to *Wilkinson Microwave Anisotropy Probe*, *WMAP*; see Hajian et al. 2011) from the ACT time-stream data is described in Dünner et al. (2013). Follow-up optical imaging observations of these clusters, using the NTT and SOAR telescopes, are reported in Menanteau et al. (2010), and Sehgal et al. (2011) discuss the cosmological constraints obtained from this sample.

In this work, we use a subset of 14 clusters from the ACT sample that have received extensive spectroscopic observations with

Table 1. Properties of the cluster sample used in this work. Masses are dynamical estimates obtained from line-of-sight velocity dispersion measurements; all values have been rescaled from R_{200} (as reported by Sifón et al. 2012) to R_{500}.

Name	z	M_{500} (10^{14} M$_\odot$)	Y_{500} (10^{-11})	y_0 (10^{-4})	R_{500} (Mpc)
ACT-CL J0102−4915	0.870	9.8 ± 2.3	9.7 ± 1.7	7.17 ± 0.88	1.1
ACT-CL J0215−5212	0.480	5.8 ± 1.7	2.0 ± 0.8	1.18 ± 0.27	1.1
ACT-CL J0232−5257	0.556	4.2 ± 1.5	1.0 ± 0.6	0.94 ± 0.27	0.9
ACT-CL J0235−5121	0.278	7.0 ± 2.1	5.0 ± 1.7	1.14 ± 0.22	1.2
ACT-CL J0237−4939	0.334	12.2 ± 2.5	2.6 ± 1.8	1.09 ± 0.31	1.4
ACT-CL J0304−4921	0.392	7.7 ± 1.8	5.8 ± 2.2	2.08 ± 0.41	1.2
ACT-CL J0330−5227	0.442	10.3 ± 2.4	4.6 ± 1.0	1.68 ± 0.24	1.3
ACT-CL J0346−5438	0.530	6.4 ± 1.4	2.8 ± 0.9	1.67 ± 0.34	1.1
ACT-CL J0438−5419	0.421	12.7 ± 3.0	7.4 ± 0.8	2.07 ± 0.17	1.4
ACT-CL J0509−5341	0.461	3.5 ± 1.4	2.6 ± 0.6	1.13 ± 0.19	0.9
ACT-CL J0528−5259	0.768	3.6 ± 1.3	0.8 ± 0.3	1.03 ± 0.28	0.8
ACT-CL J0546−5345	1.066	4.8 ± 2.5	1.7 ± 0.3	2.54 ± 0.39	0.8
ACT-CL J0559−5249	0.609	8.9 ± 2.6	2.4 ± 0.5	1.48 ± 0.23	1.2
ACT-CL J0616−5227	0.684	6.8 ± 2.9	2.5 ± 0.5	1.87 ± 0.28	1.0

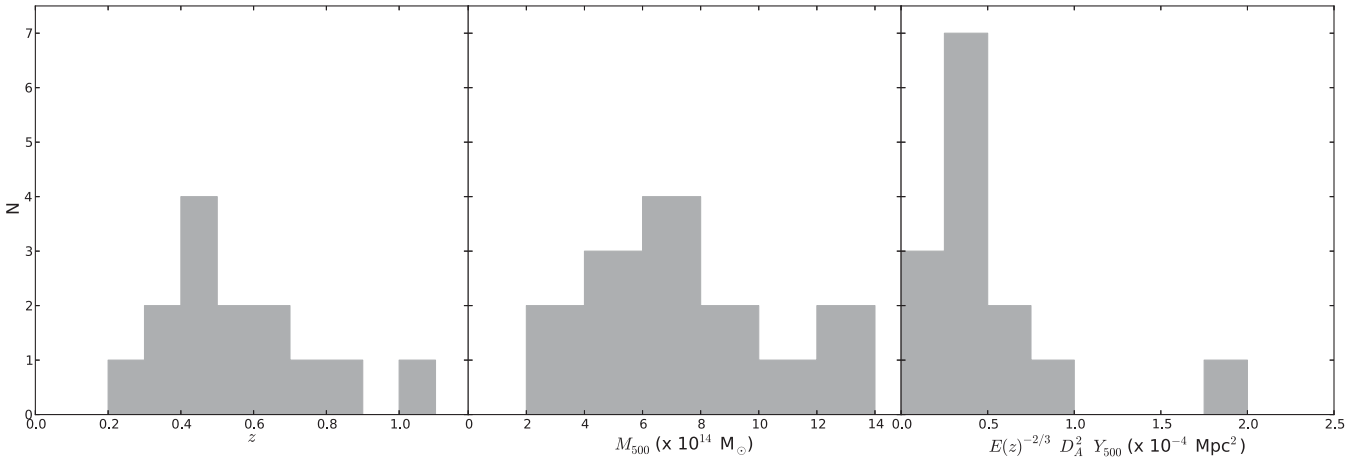

Figure 1. Redshift, dynamical mass and Y_{500} distributions for the Sunyaev–Zel'dovich effect selected cluster sample used in this work (see Sifón et al. 2012, for details). The clear outlier in the Y_{500} distribution is the $z = 0.87$ merger system ACT-CL J0102−4915 ('El Gordo'; see Menanteau et al. 2012).

Gemini-South and the Very Large Telescope (Sifón et al. 2012). On average, redshifts were measured for 60 galaxies per cluster, resulting in dynamical mass estimates with a typical uncertainty of about 30 per cent. These measurements were used to investigate the mass scaling relation with the SZ signal characterized using three different methods. We use two of these types of measurements in this paper; both are described in detail in Hasselfield et al. (2013). The first is the dimensionless, matched filter SZ amplitude (y_0), which is extracted from maps filtered using an Arnaud et al. (2010) profile with a fixed angular scale $\theta_{500} = 5.9$ arcmin, and subsequently corrected to the angular scale corresponding to R_{500} at the observed cluster redshift as described in Hasselfield et al. Our second estimate is the widely used, spherically integrated Compton signal (Y_{500}), measured within the radius R_{500}. It is important to note that both of these measurements ultimately derive from the matched filter amplitude, and are therefore highly correlated with each other and dependent upon the assumed Arnaud et al. (2010) model for the cluster SZ signal. We use the updated Y_{500} and y_0 values presented in the appendix of Hasselfield et al.; these were measured using improved ACT maps which include data obtained in the 2009–2010 observing seasons.

Note that because our Infrared Array Camera (IRAC) data do not cover out to R_{200} for the lower redshift objects in our sample (see Section 2.2), we rescale the measurements of Sifón et al. (2012) at R_{200}–R_{500} using the concentration–mass relation of Duffy et al. (2008). We include the uncertainty introduced by the scatter in this relation in the error bars on the M_{500} measurements. This results in the fractional mass errors being approximately 9 per cent larger than the uncertainties quoted in Sifón et al. (2012). Table 1 lists the cluster properties.

Fig. 1 shows the redshift, mass and Y_{500} distributions for the clusters used in this work. The sample spans the redshift range $0.27 < z < 1.07$, with median $z = 0.50$, and has median mass $M_{500} = 6.9 \times 10^{14}$ M$_\odot$. The object with the largest intrinsic Y_{500}, which is a clear outlier from the distribution shown in the right-hand panel of Fig. 1, is the spectacular 'El Gordo' (ACT-CL J0102−4915) merger system at $z = 0.87$, for which we have previously published a detailed multiwavelength analysis (Menanteau et al. 2012).

2.2 *Spitzer* IRAC imaging and photometry

We obtained IRAC 3.6 and 4.5 μm observations of the cluster sample during the period of 2010 August–December (programme ID: 70149, PI: Menanteau), using a 2×2 grid of IRAC pointings centred on each cluster position. A total of 10×100 s frames were obtained in each channel at each grid position, using a large-scale

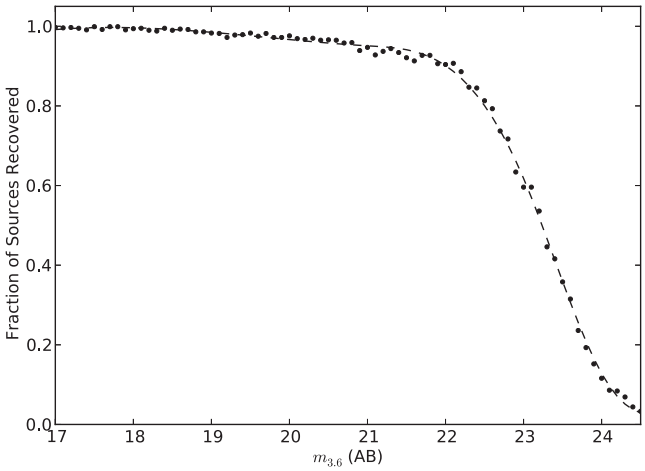

Figure 2. Fraction of synthetic point sources recovered as a function of magnitude in the 3.6 μm channel. The dashed line is a spline fit to the data. The 80 per cent completeness depth is approximately 22.6 mag.

cycling dither pattern. The basic calibrated data (BCD) images were corrected for pulldown using the software of Ashby & Hora,[1] and then mosaicked using MOPEX (Makovoz & Khan 2005) to provide images which are ≈13 arcmin on a side with 0.6 arcsec pixel scale. The mosaics for each channel were then registered to a common pixel coordinate system. These mosaics cover out to R_{500} for every cluster in the sample. By inserting synthetic point sources, we estimate the 80 per cent completeness depths of the final maps to be ≈22.6 mag (AB) in both channels (see Fig. 2).

Matched aperture photometry was performed on the IRAC maps using SEXTRACTOR (Bertin & Arnouts 1996) in dual image mode, using the 3.6 μm channel as the detection band. We measure fluxes through 4 arcsec diameter circular apertures, which are corrected to estimates of total magnitude using aperture corrections (as measured by Barmby et al. 2008) of -0.35 ± 0.04 and -0.37 ± 0.04 mag in the 3.6 and 4.5 μm channels, respectively. The photometric uncertainties were scaled upwards by factors of 2.8 and 2.6 in the 3.6 and 4.5 μm channels, respectively, in order to account for noise correlation between pixels introduced in the production of the mosaics which is not taken into account in the SEXTRACTOR error estimates. These scaling factors were determined using the method outlined in Barmby et al. (2008). Finally, the uncertainties in the aperture corrections were added to the photometric errors in quadrature.

The BCGs are extended objects for which the aperture-corrected point-source magnitudes are not good approximations to the total flux. We therefore use the SEXTRACTOR MAG_AUTO magnitudes, again scaling up the photometric uncertainties using the method of Barmby et al. (2008). Note that we do not attempt to deblend the BCGs beyond the level provided by SEXTRACTOR. While it is possible to use more sophisticated techniques to improve deblending using higher resolution imaging at other wavelengths (e.g. TFIT; Laidler et al. 2007), we only possess relatively shallow ground-based optical data for the objects in our sample, which would require a large *k*-correction to IRAC wavelengths.

[1] See http://irsa.ipac.caltech.edu/data/SPITZER/docs/dataanalysistools/tools/contributed/irac/fixpulldown/.

3 INFRARED LUMINOSITY FUNCTIONS

The LF encodes key information about galaxy populations, and has been used to characterize the variation of galaxy properties with environment (e.g. Blanton et al. 2003; De Propris et al. 2003; Croton et al. 2005; Popesso et al. 2006; Loveday et al. 2012) and redshift (e.g. De Propris et al. 1999; Lin et al. 2006; Muzzin et al. 2008; Mancone et al. 2010; Capozzi et al. 2012). Since the IRAC photometry probes the peak of the stellar light, the IR LF serves as a good proxy for the stellar mass function. In this section, we present the first measurements of the IR galaxy LFs of SZ-selected clusters and compare our results to those found from IR-selected cluster samples.

3.1 Method

We divide the cluster sample by redshift into two equal-sized subsamples ($0.2 < z < 0.5$ and $0.5 < z < 1.1$) and measure their composite LFs within R_{500}. Although we have a large sample of spectroscopic redshifts for each cluster in addition to optical photometry, in most cases the optical data do not provide coverage out to R_{500}. Therefore, we use statistical background subtraction to ensure consistency in our analysis across all the objects in the sample. This lack of optical data for some regions of most of the cluster fields, coupled to the low resolution of the IRAC images, makes star–galaxy separation difficult. Following Lin et al. (2012), we remove the brightest stars by cross-matching the IRAC catalogues with the Two Micron All Sky Survey (2MASS) point-source catalogue (using a 2 arcsec matching radius); this should reduce the stellar contamination to around the 7 per cent level (Lin et al. 2012). We also remove all objects brighter than the BCG in each field, which further reduces stellar contamination. Remaining stars are removed statistically during subtraction of the background sample. Since our IRAC cluster images do not extend to a large radius beyond R_{500}, we use the IRAC source catalogue of the Extended Groth Strip (EGS; Barmby et al. 2008) as the background field sample. We treat the EGS catalogue in the same manner as our IRAC catalogues of the cluster fields throughout (including, for example, removing most stellar contamination by cross matching with 2MASS). We mask out areas around very bright stars in some of our cluster fields and take the reduction in area into account when subtracting the background contribution.

We compute the composite LFs for each subsample using the method of Colless (1989). We use the aperture-corrected magnitudes (see Section 2.2) in the observed frame and exclude the BCGs since they are not drawn from the same population as ordinary cluster galaxies (e.g. Tremaine & Richstone 1977; Loh & Strauss 2006; Lin, Ostriker & Miller 2010). We apply a modest completeness correction (approximately 10 per cent for $21.5 < m_{3.6} < 22.0$), estimated from inserting synthetic point sources into our images (see Section 2.2). For the background sample from EGS, which reaches similar depth to our observations, we use table 5 of Barmby et al. (2008) to model the completeness as a function of magnitude. For each cluster in each subsample, we *k*-correct its magnitudes [assuming a $\tau = 0.1$ Gyr single-burst Bruzual & Charlot (2003, BC03 hereafter) model, formed at $z_f = 3$ with solar metallicity] to the median redshift of the subsample, and take into account the distance modulus between each cluster and that median redshift (see, e.g. Muzzin et al. 2008; Mancone et al. 2010; Lin et al. 2012). The *k*- and distance modulus corrections adopted for each cluster are listed in Table 2. We divide the data into bins of width 0.5 mag and then perform the same operations on the background galaxy

Table 2. Distance modulus (DM_{corr}) and k-corrections applied to cluster photometry to correct each object to the median redshift of the appropriate subsample. The correction applied is as follows: corrected magnitude = observed apparent magnitude $+k+$ DM_{corr}, where k is the k-correction in either the 3.6 or 4.5 μm bands ($k_{3.6}$ and $k_{4.5}$, respectively). See Section 3.1 for details.

Cluster	z	$k_{3.6}$	$k_{4.5}$	DM_{corr}
Low-redshift subsample (median $z = 0.42$):				
ACT-CL J0509−5341	0.461	+0.102	+0.054	−0.231
ACT-CL J0330−5227	0.442	+0.053	+0.028	−0.121
ACT-CL J0438−5419	0.421	+0.000	+0.000	+0.000
ACT-CL J0215−5212	0.480	+0.151	+0.080	−0.337
ACT-CL J0304−4921	0.392	−0.076	−0.041	+0.184
ACT-CL J0237−4939	0.334	−0.202	−0.125	+0.590
ACT-CL J0235−5121	0.278	−0.304	−0.215	+1.056
High-redshift subsample (median $z = 0.68$):				
ACT-CL J0346−5438	0.530	−0.329	−0.182	+0.673
ACT-CL J0102−4915	0.870	+0.245	+0.340	−0.642
ACT-CL J0616−5227	0.684	+0.000	+0.000	+0.000
ACT-CL J0528−5259	0.768	+0.115	+0.140	−0.308
ACT-CL J0546−5345	1.066	+0.436	+0.690	−1.188
ACT-CL J0232−5257	0.556	−0.262	−0.151	+0.546
ACT-CL J0559−5249	0.609	−0.140	−0.097	+0.306

sample, before subtracting the area-scaled background contribution in each bin.

We fit Schechter (1976) functions to the composite LFs using χ^2 minimization. We fit for both the characteristic magnitude (m^*) and the faint-end slope (α), although we also perform fits with α fixed to other values common in the literature (e.g. $\alpha = -0.8$), in order to simplify the comparison with other works (since m^* and α are degenerate). The normalization of the Schechter function fit is fixed such that its integral is equal to the number of galaxies in the composite LF.

3.2 Results

Fig. 3 shows the LFs in each IRAC channel for both the low- and high-redshift subsamples. The values of m^* that we derive in both channels for the $\langle z \rangle = 0.42$ subsample agree at better than 1σ with measurements of m^* in IR-selected cluster samples by Muzzin et al. (2008) and Mancone et al. (2010) at similar redshift (note that the faint-end slope, α, was fixed to -0.8 in these works). We find a slightly brighter m^* for the $\langle z \rangle = 0.68$ subsample ($m^*_{3.6} = 19.26 \pm 0.07$ for $\alpha = -0.8$) in comparison to both Muzzin et al. (2008) and Mancone et al. (2010), although all values are consistent at better than the 2σ level. If this difference is real, it may reflect a different time-scale for the build up of the bright end of the LF between the samples, with more massive galaxies being assembled at earlier times in more massive clusters (since we expect the average mass of the SZ-selected sample to be significantly larger than that of the IR-selected samples, which are drawn from a smaller survey area). Fig. 4 illustrates the evolution of $m^*_{3.6}$ in the Mancone et al. (2010) sample in comparison to our results. We also see reasonable agreement between m^* measured for our $\langle z \rangle = 0.68$ subsample and

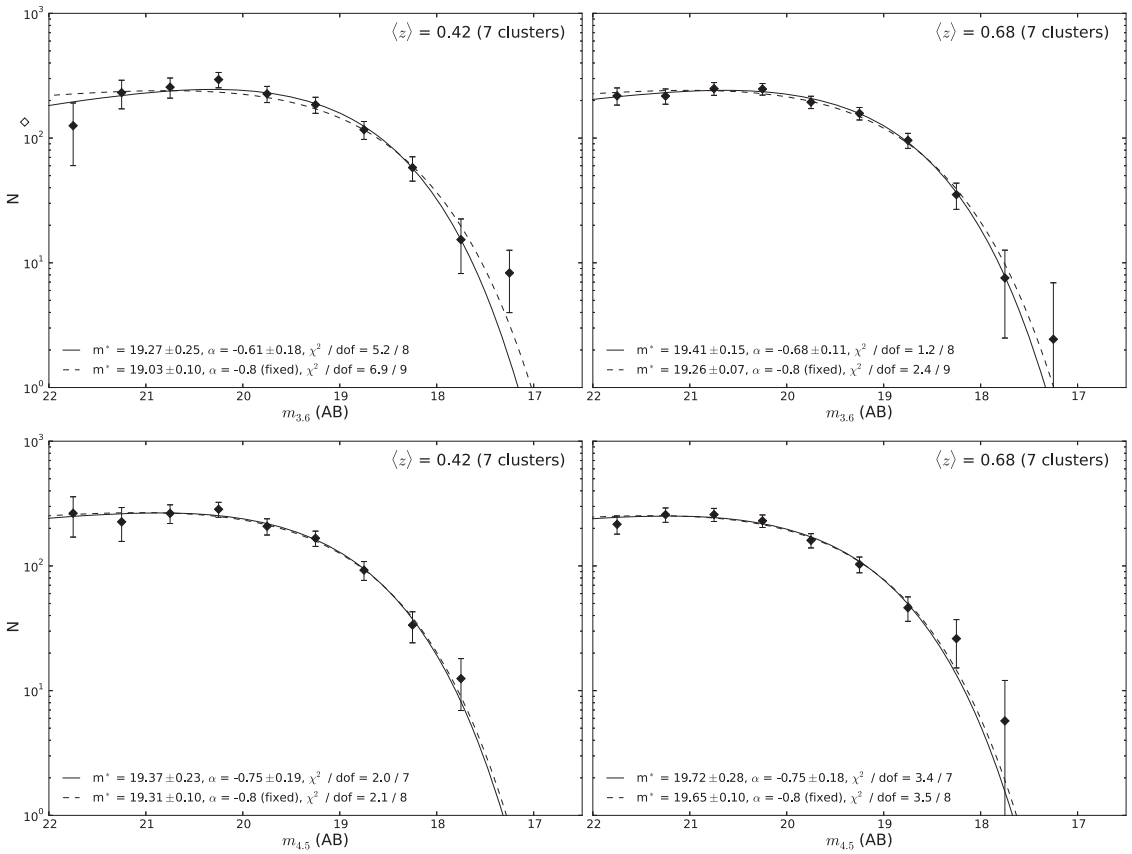

Figure 3. Composite luminosity functions of ACT Sunyaev–Zel'dovich effect selected galaxy clusters in two redshift bins, for each IRAC channel. The solid curve shows the best-fitting Schechter function with m^* and α as free parameters, while the dashed curve shows the best fit with α fixed at -0.8.

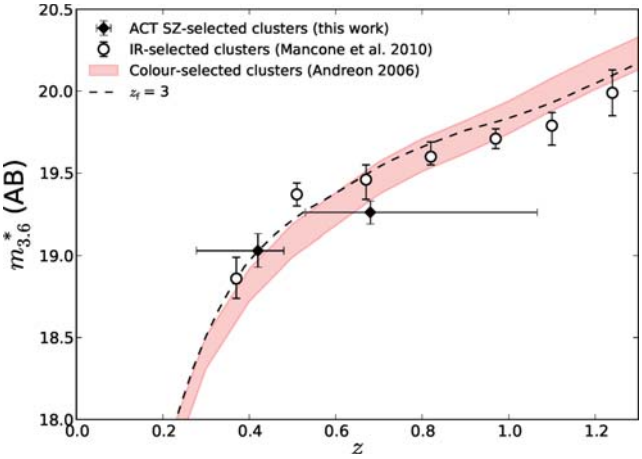

Figure 4. Comparison of $m^*_{3.6}$ found from the SZ-selected cluster sample used in this work with results for an IR-selected cluster sample (Mancone et al. 2010). In both cases, the faint-end slope is fixed to $\alpha = -0.8$. There is reasonable agreement, which suggests that the galaxy populations in each sample are not likely to be significantly different, although $m^*_{3.6}$ for the $\langle z \rangle = 0.68$ subsample of SZ-selected clusters is approximately 0.3 mag brighter. The dashed line shows the expected evolution of a solar metallicity (Bruzual & Charlot 2003) $\tau = 0.1$ Gyr single-burst stellar population model formed at $z_f = 3$, normalized to the Mancone et al. (2010) measurement at $z = 0.37$. The horizontal error bars mark the redshift ranges covered by the ACT subsamples.

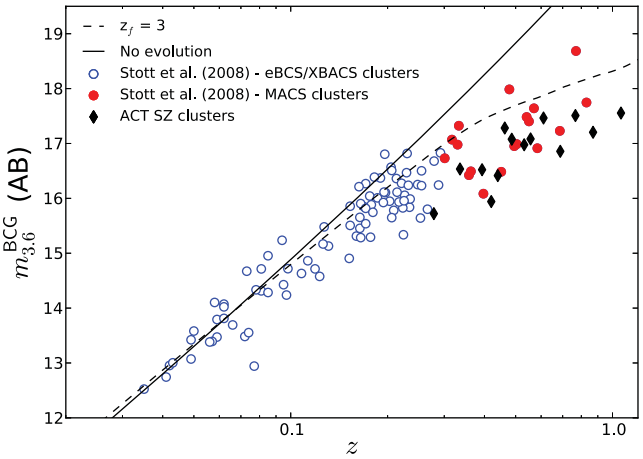

Figure 5. Hubble diagram of BCGs in ACT clusters (black diamonds) in the 3.6 μm IRAC channel. The *K*-band observations (*k*-corrected to the IRAC 3.6 μm channel assuming a $\tau = 0.1$ Gyr single-burst, solar metallicity, Bruzual & Charlot (2003) model formed at $z_f = 3$) of two samples of X-ray-selected clusters (Ebeling et al. 1996, 2000; Ebeling, Edge & Henry 2001) by Stott et al. (2008) are shown for comparison. The dashed line shows the expected evolution for the same Bruzual & Charlot (2003) model used to perform the *k*-correction, while the solid line shows the no-evolution line; both of these are normalized to match the data at $z < 0.1$.

the results of De Propris et al. (2007) at $\langle z \rangle = 0.75$, when we set $\alpha = -0.25$, as was found in that work.

The faint-end slopes that we find while fitting for both m^* and α are consistent with that measured by Lin, Mohr & Stanford (2004) in the *K* band from a heterogeneous sample of X-ray-selected clusters at $z = 0.1$, who found $\alpha = -0.84 \pm 0.02$, although we note that the uncertainties on our measurements are much larger. We conclude that the IR LFs of SZ-selected clusters do not differ significantly from clusters selected using other methods.

4 BRIGHTEST CLUSTER GALAXIES

4.1 The Hubble diagram

BCGs are the brightest galaxies in the Universe in terms of their stellar emission, and early work recognized their potential as standard candles, using their Hubble diagram to estimate the deceleration parameter (e.g. Sandage 1972). More recently, the Hubble diagram of BCGs has been used to study their mass growth (e.g. Aragon-Salamanca, Baugh & Kauffmann 1998; Burke, Collins & Mann 2000; Brough et al. 2002). Some semi-analytic models predict that BCGs should have acquired about 80 per cent of their stellar mass since $z \sim 1$ through accretion and merging (De Lucia & Blaizot 2007), although recent observations of BCGs in both high-redshift optical and X-ray-selected clusters show that most of the stellar mass in these objects was already assembled by $z \sim 1$ (e.g. Brough et al. 2008; Whiley et al. 2008; Collins et al. 2009; Stott et al. 2010; Lidman et al. 2012).

Fig. 5 presents the 3.6 μm Hubble diagram of BCGs in the ACT SZ-selected sample, in comparison to *K*-band observations of X-ray-selected clusters (*k*-corrected to 3.6 μm, assuming a $\tau = 0.1$ Gyr single-burst, solar metallicity, BC03 model formed at $z_f = 3$), taken from Stott et al. (2008, who measure total BCG magnitudes, as in this work). One of the X-ray samples to which we compare is the Massive Cluster Survey (MACS; Ebeling et al. 2007, 2010), which is extracted from the *ROSAT* All Sky Survey (Voges et al. 1999), and probes a similar mass and redshift range to the ACT sample. Although we have normalized the evolution tracks shown in this figure to match the low-redshift BCG sample, it should be noted that the massive ACT clusters will not evolve to have similar masses to the low-redshift clusters.

To check if the ACT and MACS BCGs trace similar populations, we convert our estimates of 3.6 μm BCG total magnitude to stellar mass, assuming a solar metallicity $\tau = 0.1$ Gyr single-burst BC03 model, formed at $z_f = 3$, and do the same for the MACS BCGs. We compare the resulting BCG stellar mass distributions using the two-sample Kolmogorov–Smirnov (KS) test. When comparing to the whole MACS sample, the KS test returns $D = 0.44$, with null hypothesis (that the samples are drawn from the same distribution) probability $p = 0.06$. Restricting both samples to include only the $0.4 < z < 1.0$ BCGs, the null hypothesis probability increases to $p = 0.4$. We conclude that the ACT and MACS BCGs are a similar population.

4.2 BCG stellar mass scaling relations

We now examine the scaling of BCG stellar mass with the properties of the ACT clusters. We convert our estimates of 3.6 μm BCG total magnitudes to stellar mass, assuming a solar metallicity $\tau = 0.1$ Gyr single-burst BC03 model, formed at $z_f = 3$. The uncertainty in the stellar mass estimates is dominated by the choice of model; since formation redshifts in the range of $2 < z_f < 5$ are reasonable for BCGs (e.g. Stott et al. 2008, 2010; Whiley et al. 2008), we adopt the stellar mass estimates inferred from models at each end of this redshift range as fiducial error bars (the impact of photometric uncertainties is negligible by comparison). We do not take into account possible systematic uncertainties, which are considerable. The largest systematic that can affect stellar mass estimates is the IMF; if we adopted a Chabrier (2003) rather than a Salpeter (1955) IMF, our stellar mass estimates would be 0.24 dex lower.

Table 3. Properties of the BCGs; $m_{3.6}$ and $m_{4.5}$ are the total apparent magnitudes (observed frame) on the AB system in the IRAC 3.6 and 4.5 μm channels, respectively; M_* is the stellar mass estimated from $m_{3.6}$ alone, assuming a $\tau = 0.1$ Gyr burst Bruzual & Charlot (2003) model with a Salpeter (1955) IMF and solar metallicity formed at $z_f = 3$. The error bars on the stellar mass estimates correspond to assumptions of $z_f = 2$ and 5 (systematic errors due to the choice of stellar population model and/or IMF are neglected).

Cluster	RA (J2000)	Dec. (J2000)	$m_{3.6}$	$m_{4.5}$	M_* (10^{11} M$_\odot$)
ACT-CL J0102−4915	$01^h02^m57^s.772$	$-49°16'19''.14$	17.204 ± 0.009	17.628 ± 0.010	$16.2^{+2.8}_{-3.4}$
ACT-CL J0215−5212	$02^h15^m12^s.229$	$-52°12'25''.09$	17.078 ± 0.006	17.349 ± 0.006	$10.9^{+0.6}_{-1.2}$
ACT-CL J0232−5257	$02^h32^m42^s.704$	$-52°57'22''.62$	17.083 ± 0.006	17.453 ± 0.007	$12.1^{+1.2}_{-1.3}$
ACT-CL J0235−5121	$02^h35^m45^s.242$	$-51°21'04''.83$	15.722 ± 0.002	15.906 ± 0.002	$17.6^{+1.1}_{-1.2}$
ACT-CL J0237−4939	$02^h37^m01^s.661$	$-49°38'09''.66$	16.535 ± 0.005	16.734 ± 0.005	$11.3^{+0.7}_{-0.8}$
ACT-CL J0304−4921	$03^h04^m16^s.132$	$-49°21'25''.97$	16.522 ± 0.004	16.724 ± 0.004	$14.4^{+0.8}_{-1.4}$
ACT-CL J0330−5227	$03^h30^m56^s.935$	$-52°28'13''.18$	16.415 ± 0.004	16.639 ± 0.004	$18.3^{+1.0}_{-2.0}$
ACT-CL J0346−5438	$03^h46^m55^s.370$	$-54°38'54''.66$	16.977 ± 0.006	17.261 ± 0.006	$12.9^{+1.1}_{-1.3}$
ACT-CL J0438−5419	$04^h38^m17^s.644$	$-54°19'20''.42$	15.942 ± 0.003	16.159 ± 0.003	$26.9^{+1.5}_{-2.7}$
ACT-CL J0509−5341	$05^h09^m21^s.375$	$-53°42'12''.79$	17.282 ± 0.010	17.554 ± 0.010	$8.6^{+0.5}_{-0.9}$
ACT-CL J0528−5259	$05^h28^m05^s.332$	$-52°59'53''.27$	17.509 ± 0.008	17.965 ± 0.009	$11.1^{+1.3}_{-2.4}$
ACT-CL J0546−5345	$05^h46^m37^s.729$	$-53°45'31''.41$	17.554 ± 0.007	17.835 ± 0.007	$13.4^{+3.3}_{-2.3}$
ACT-CL J0559−5249	$05^h59^m43^s.230$	$-52°49'27''.05$	17.464 ± 0.008	17.873 ± 0.010	$9.2^{+1.0}_{-1.3}$
ACT-CL J0616−5227	$06^h16^m34^s.090$	$-52°27'08''.94$	16.857 ± 0.004	17.374 ± 0.004	$18.1^{+1.7}_{-3.0}$

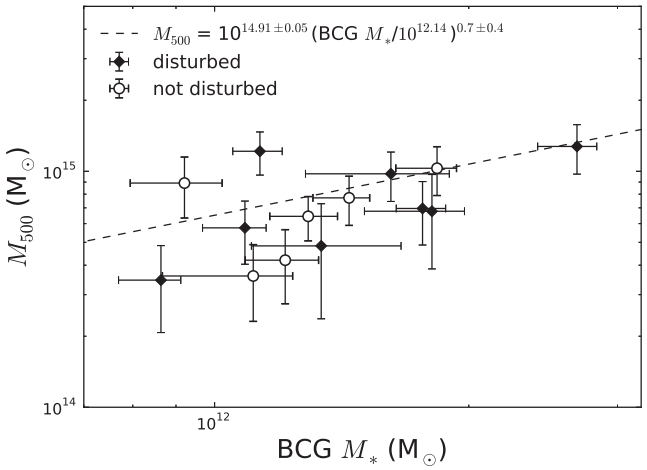

Figure 6. Scaling relation between BCG stellar mass and cluster dynamical mass. The dashed line is a regression fit to the data using the Kelly (2007) method. There is no evidence from this small sample that disturbed clusters (black diamonds; defined according to the criteria described in Sifón et al. 2012) follow a different trend from non-disturbed clusters (white circles).

Similarly, adopting stellar population models with a larger contribution to the IR flux by thermally pulsating asymptotic giant branch stars (e.g. Maraston 2005; Conroy, Gunn & White 2009) would result in smaller stellar masses. Table 3 lists the BCG magnitudes and stellar mass estimates derived using our adopted BC03 model.

Fig. 6 presents the relation between BCG stellar mass and cluster dynamical mass. We find mild evidence for a correlation, with Spearman rank coefficient $\rho = 0.56$ and null hypothesis (i.e. no correlation) probability $p = 0.04$. Using the Markov chain Monte Carlo (MCMC) based method of Kelly (2007), we find that the slope of the relation is shallow and poorly constrained ($M_{500} \propto M_*^{0.7 \pm 0.4}$). The intrinsic scatter in the relation at fixed BCG M_* is $\sigma_{\log M_{500}} = 0.14 \pm 0.06$.

Many other studies have previously found a correlation between BCG luminosity and cluster mass using X-ray-selected and optically selected cluster samples (e.g. Lin & Mohr 2004; Popesso et al. 2007; Brough et al. 2008; Yang, Mo & van den Bosch 2008; Mittal et al. 2009). Like Haarsma et al. (2010), the correlation we find is only marginally significant; presumably this is due to the small sample size. For example, Whiley et al. (2008) found a correlation between BCG K-band magnitude and cluster velocity dispersion (i.e. a comparable proxy to the dynamical mass estimates used in this work), significant at the 99.9 per cent level, for a sample of 81 optically selected clusters in the $0.02 < z < 0.96$ redshift range. We note that the wide redshift range covered by our sample may also be a contributing factor, if the relation evolves with redshift.

Fig. 7 shows the relations between BCG stellar mass and SZ signal, Y_{500} and y_0. These are the first measurements of these relations. In these cases we find stronger evidence for correlation with the BCG stellar mass. For the scaling with Y_{500}, we find Spearman rank coefficient $\rho = 0.66$, with null hypothesis probability $p = 0.01$. Applying the Kelly (2007) regression method, the slope of the relation is $E(z)^{-2/3}\, D_A^2\, Y_{500} \propto M_*^{1.2 \pm 0.6}$, with an intrinsic scatter $\sigma_{\log Y_{500}} = 0.25 \pm 0.08$. For the BCG $M_* - y_0$ relation, we find Spearman $\rho = 0.74$, with $p = 0.002$. The slope of the relation is $E(z)^{-2}\, y_0 \propto M_*^{0.8 \pm 0.4}$, and the intrinsic scatter is $\sigma_{\log y_0} = 0.18 \pm 0.05$. We note that 'El Gordo' (J0102−4915), the cluster with the largest y_0 and Y_{500} value, is a clear outlier in these plots. However, removing this object has no significant effect on the fit results.

The extensive spectroscopic data obtained on each cluster allow their dynamical states to be classified using three different methods, as described in Sifón et al. (2012). A cluster is flagged as dynamically disturbed if it satisfies any two of (i) BCG peculiar velocity different from zero at more than the 2σ level, (ii) BCG projected offset from the SZ peak cluster position more than $0.2R_{200}$ and (iii) greater than 5 per cent significance level in the Dressler & Shectman (1988) test for substructure. In both Figs 6 and 7, we show disturbed and non-disturbed clusters with different symbols, and see no evidence for different scaling of M_{500}, Y_{500} or y_0 with BCG stellar mass for clusters with different dynamical states, though of course the sample size is small.

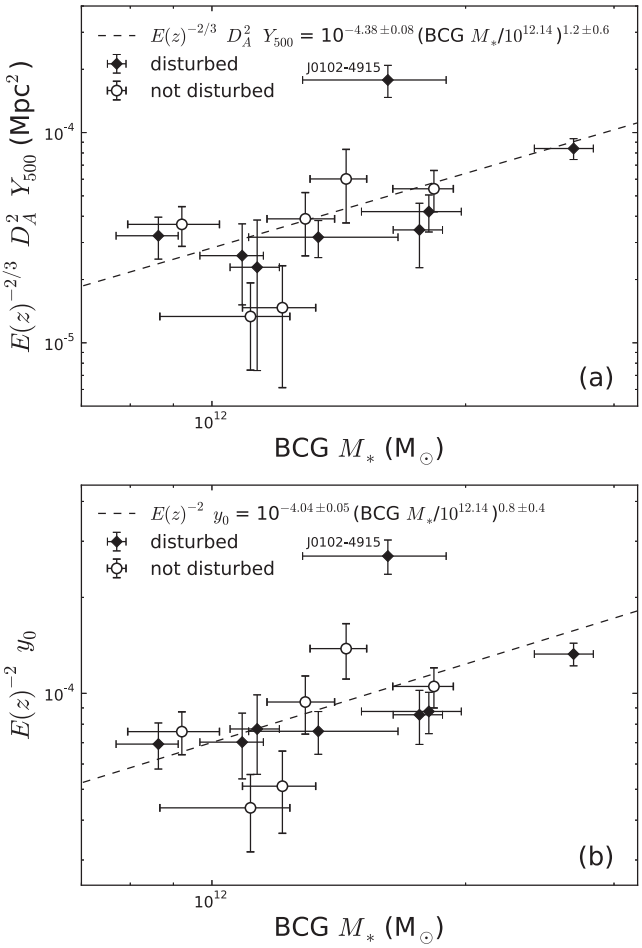

Figure 7. Scaling relations between SZ signal and BCG stellar mass: (a) scaling with Y_{500}; (b) scaling with y_0. Self-similar evolution of the SZ signal with redshift is assumed. In each panel the dashed line is a fit to the data using the Kelly (2007) regression method. We do not see different trends for disturbed (black diamonds; defined according to the criteria described in Sifón et al. 2012) and non-disturbed clusters (white circles).

5 CLUSTER STELLAR MASS SCALING RELATIONS

In this section, we examine the scaling relations between total stellar mass within R_{500} ($M_{500}^{\rm star}$), cluster dynamical mass and SZ signal.

5.1 Method

We estimate the contribution to the total light within R_{500} from cluster galaxies other than the BCG via the procedure used to measure the composite LFs (Section 3). We sum the flux from the background-subtracted number counts for each cluster down to a limit of m^*+2 (where m^* is the value obtained for the fit to the appropriate composite LF). We add a contribution for galaxies fainter than our detection limit by extrapolating the LF to m^*+5, assuming that $\alpha=-0.8$ (this correction adds less than 10 per cent to the final stellar masses). We then convert the total flux (adding in the contribution from the BCG, see Section 4) into an observed frame 3.6 μm magnitude, taking into account the difference in distance modulus and k-corrections that were applied in estimating the composite LF (recall that we previously k-corrected the photometry for each cluster in a subsample to the median redshift of that subsample; see Table 2). The stellar mass is then estimated assuming the same $z_f=3$ BC03 model applied in Sections 3 and 4. Finally, to obtain spherically deprojected values, we multiply the total stellar mass estimates by 0.73. This deprojection factor is obtained assuming an NFW profile (Navarro, Frenk & White 1997) with $c=2.8$ (the average obtained from applying the Duffy et al. (2008) $c-M_{200}$ relation to the dynamical mass estimates), and integrating to $3R_{500}$ along the line of sight. Note that our measurement does not include any contribution from the intracluster light (ICL). Table 4 lists the $M_{500}^{\rm star}$ value for each cluster.

Table 4. Cluster total 3.6 μm magnitudes (observed frame) and total stellar mass ($M_{500}^{\rm star}$) estimated within R_{500}. The stellar mass conversion is performed as described in Section 4.2 for the BCGs, and the same caveats noted in the caption to Table 3 apply. Note that any contribution to $M_{500}^{\rm star}$ from the ICL is not accounted for.

Cluster	z	$m_{3.6}$	$M_{500}^{\rm star}$ (10^{12} $\mathrm{M}_\odot$)
ACT-CL J0102−4915	0.870	14.22 ± 0.09	$18.8^{+3.5}_{-4.1}$
ACT-CL J0215−5212	0.480	14.54 ± 0.09	$8.5^{+0.8}_{-1.1}$
ACT-CL J0232−5257	0.556	14.34 ± 0.07	$11.4^{+1.5}_{-1.5}$
ACT-CL J0235−5121	0.278	12.85 ± 0.03	$18.6^{+1.6}_{-1.6}$
ACT-CL J0237−4939	0.334	14.26 ± 0.10	$7.0^{+1.0}_{-1.0}$
ACT-CL J0304−4921	0.392	14.02 ± 0.07	$10.9^{+1.0}_{-1.3}$
ACT-CL J0330−5227	0.442	13.44 ± 0.07	$21.2^{+1.8}_{-2.6}$
ACT-CL J0346−5438	0.530	14.07 ± 0.06	$14.0^{+1.6}_{-1.7}$
ACT-CL J0438−5419	0.421	13.30 ± 0.06	$23.1^{+1.8}_{-2.7}$
ACT-CL J0509−5341	0.461	14.48 ± 0.11	$8.6^{+1.0}_{-1.2}$
ACT-CL J0528−5259	0.768	14.59 ± 0.11	$12.2^{+1.8}_{-2.9}$
ACT-CL J0546−5345	1.066	14.50 ± 0.14	$16.6^{+4.2}_{-3.1}$
ACT-CL J0559−5249	0.609	13.74 ± 0.06	$21.1^{+2.7}_{-3.2}$
ACT-CL J0616−5227	0.684	13.94 ± 0.08	$19.9^{+2.3}_{-3.6}$

5.2 Results

Fig. 8 shows the scaling of $M_{500}^{\rm star}$ with dynamical mass. While there is some evidence of a correlation in this plot, we find that J0237−4939

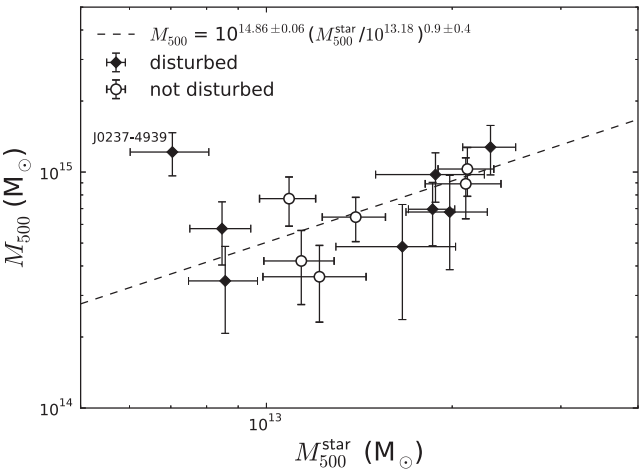

Figure 8. Scaling relation between total stellar mass ($M_{500}^{\rm star}$) and dynamical cluster mass (M_{500}). The dashed line indicates the fit obtained with the Kelly (2007) regression method, after excluding the outlier J0237−4939, which has a very low stellar mass compared to its dynamical mass. *Chandra* X-ray observations of this cluster indicate that its dynamical mass may be overestimated.

is a clear outlier, as it has the smallest $M_{500}^{\rm star}$ in the sample but is the second ranked cluster in the sample in terms of its dynamical mass. A preliminary analysis of the *Chandra* X-ray data for this system indicates that the dynamical mass is likely overestimated – the X-ray temperature is $T = 5.3^{+0.8}_{-0.7}$ keV, which implies mass $M_{500} = (4.0 \pm 1.0) \times 10^{14}$ M$_\odot$ (assuming the Vikhlinin et al. 2009 $M-T$ relation). This is roughly one-third of the dynamical mass for this system as listed in Table 1. A full comparison of dynamical versus X-ray-derived mass estimates for the ACT sample will be presented in a future paper (Hughes et al., in preparation).

If this cluster is excluded, we obtain Spearman rank coefficient $\rho = 0.76$ with null hypothesis probability $p = 0.002$. Applying the Kelly (2007) regression method with J0237 excluded, we find the relation $M_{500} \propto M_{500}^{\rm star\ 0.9\pm0.4}$, with an intrinsic scatter $\sigma_{\log M_{500}} = 0.10 \pm 0.06$. If J0237 is included in the sample, the correlation is not significant ($\rho = 0.47$, $p = 0.09$) and a much shallower slope for the relation is inferred ($M_{500} \propto M_{500}^{\rm star\ 0.3\pm0.4}$).

We present the relations between $M_{500}^{\rm star}$ and SZ signal (y_0, Y_{500}) in Fig. 9. In both cases we see a correlation, although the Spearman rank test indicates that the correlation with Y_{500} is more significant ($\rho = 0.63$, $p = 0.02$) compared to the correlation with y_0 ($\rho = 0.46$, $p = 0.10$). In both cases, as with the scaling with the BCG stellar mass, the slopes of the relations are poorly constrained [$E(z)^{-2/3}\ D_A^2\ Y_{500} \propto M_{500}^{\rm star\ 1.0\pm0.6}$; $E(z)^{-2}\ y_0 \propto M_{500}^{\rm star\ 0.5\pm0.4}$] with large intrinsic scatter ($\sigma_{\log Y_{500}} = 0.26 \pm 0.09$; $\sigma_{\log y_0} = 0.20 \pm 0.06$).

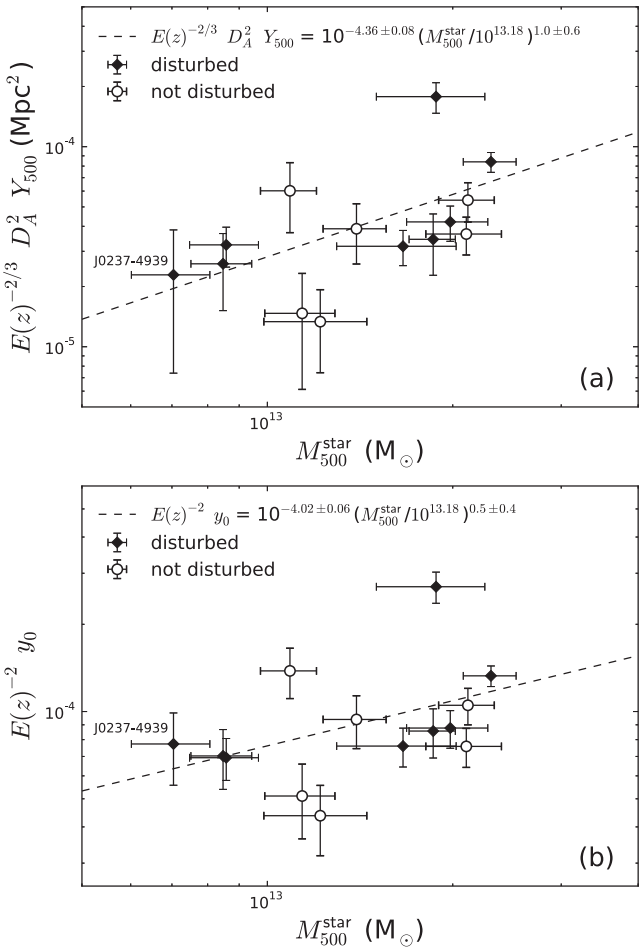

Figure 9. Scaling relations between SZ signal and cluster stellar mass: (a) scaling with Y_{500} and (b) scaling with y_0. Self-similar evolution is assumed in both cases. The dashed line indicates the fit obtained using the Kelly (2007) regression method. J0237−4939, which has a very low stellar mass compared to its dynamical mass (see Section 5.2), is not an outlier in either relation.

Despite the fact that J0237 is an outlier in the scaling of $M_{500}^{\rm star}$ with dynamical mass, it is not an outlier in either of the SZ-signal relations. If we exclude it from the sample, we find less than 1σ shifts in all of the fit parameters and statistics quoted above for both the y_0–$M_{500}^{\rm star}$ and Y_{500}–$M_{500}^{\rm star}$ scaling relations.

6 DISCUSSION

We now discuss the variation of the baryon fraction in stars ($f_{500}^{\rm star} = M_{500}^{\rm star}/M_{500}$) with cluster mass for the ACT SZ-selected sample. This relationship may provide some insight into the role of feedback in regulating star formation efficiency in clusters (e.g. Bode et al. 2009).

Fig. 10 shows our results in comparison to a number of works in the literature. For the ACT sample, we find $f_{500}^{\rm star}$ values that span the range 0.006–0.034, with median 0.022. The cluster at the low end of this range is J0237−4939, which has an unusually low stellar mass given its dynamical mass (although as noted above, analysis of the X-ray data for this system indicates that the dynamical mass is overestimated). It is flagged as a disturbed cluster according to the criteria used by Sifón et al. (2012, note that this is also indicated by the morphology of the cluster in *Chandra* X-ray imaging), although the other disturbed clusters in the sample do not exhibit such low $f_{500}^{\rm star}$ values. In Fig. 10, we see the decreasing trend of $f_{500}^{\rm star}$ with increasing cluster mass seen in other works, though the mass range covered by the ACT sample is relatively narrow. The $f_{500}^{\rm star}$ values we find are typically slightly larger at a given mass in comparison to the results of other studies shown in the plot. While this could be a real difference, there are several possible sources of systematic error, or differences in the analyses or assumptions applied in each study, which could account for this.

The single largest source of systematic error is the choice of IMF. Here, we have adopted the Salpeter (1955) IMF (as did the work of Giodini et al. 2009), and in Fig. 10 we have rescaled the results of Lin et al. (2012) from the Kroupa (2001) IMF assumed in that work to Salpeter by adding 0.13 dex to their $M_{500}^{\rm star}$ values. If we had instead adopted a Chabrier (2003) IMF instead of Salpeter, our stellar mass measurements would be 0.24 dex lower. Gonzalez et al. (2007) took a different approach, converting light to stellar mass using an empirically determined sub-Salpeter mass-to-light ratio (M/L) ratio taken from observations of local ellipticals and S0s by Cappellari et al. (2006). We note that the possible variation of the IMF according to galaxy type is currently under debate; some recent studies (van Dokkum & Conroy 2010; Cappellari et al. 2012) suggest that early-type galaxies have a more bottom-heavy IMF relative to late-type galaxies. Accounting for such an effect is beyond the scope of this paper.

In a similar way, the assumption made in converting light to mass is also a potential source of systematic error. In the absence of multi-band photometry covering the entire sample out to R_{500}, we have simply assumed a constant M/L for each cluster, assuming all member galaxies to be represented by a single-burst BC03 model with $z_f = 3$. This is motivated by the fact that early-type galaxies form the dominant population in massive clusters, even beyond $z > 1$, with the scatter about the red sequence in such clusters being consistent with the bulk of star formation having taken place at $z \approx 3$ (e.g. Hilton et al. 2009; Mei et al. 2009; Strazzullo et al.

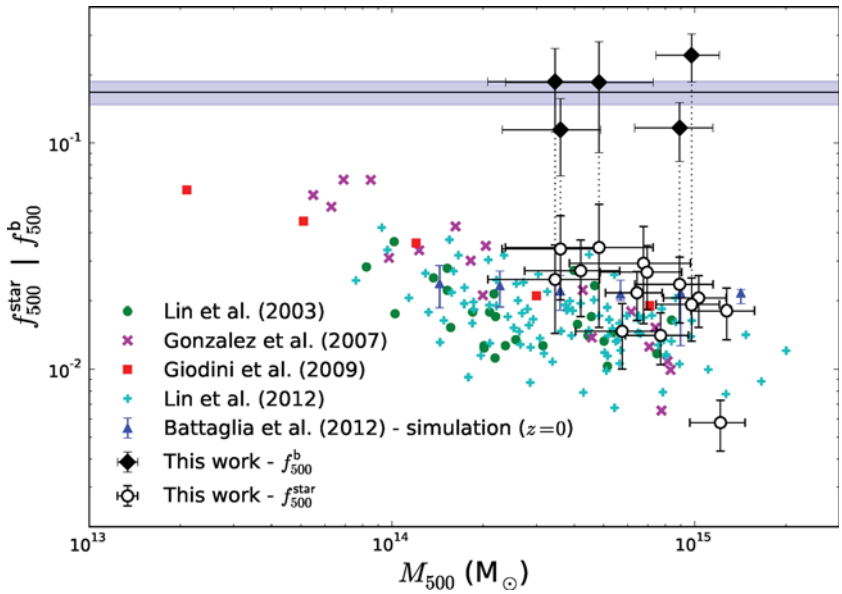

Figure 10. Fraction of the total cluster mass in stars ($f^{\rm star}_{500}$) or total baryon fraction ($f^{\rm b}_{500}$, i.e. $M^{\rm star}_{500}$ plus gas mass, where available) within R_{500}, as a function of cluster mass. The solid line marks the cosmic baryon fraction (Komatsu et al. 2011, the shaded area indicates the uncertainty). The legend indicates measurements of $f^{\rm star}_{500}$ from the literature (error bars are omitted for clarity); note that the results of Lin et al. (2012) are scaled up from a Kroupa (2001) IMF by adding 0.13 dex to the total stellar masses. Only the work of Gonzalez et al. (2007) includes the contribution from the ICL. The five black diamonds indicate $f^{\rm b}_{500}$ estimates for J0102−4915 (gas mass measurement taken from Menanteau et al. 2012), J0509−5341, J0528−5259, J0546−5345 and J0559−5249 (gas mass measurements taken from Andersson et al. 2011).

2010). This assumption is also made in Lin et al. (2012), and there is reasonable agreement between the two studies in the mass range of overlap. However, some other studies take into account the variation in M/L with galaxy type. Giodini et al. (2009) apply the $K_{\rm s}$-to-stellar mass relations of Arnouts et al. (2007), which are derived from spectral energy distribution (SED) fitting to multi-band photometry, according to galaxy colour. Leauthaud et al. (2012) used SED fitting to COSMOS photometry to obtain stellar mass estimates for each individual galaxy and estimated the stellar fraction using a statistical halo occupation distribution model approach, finding much lower values (by a factor of 2–5) than for other studies, including ours [although much of this difference can be attributed to the adoption of the Chabrier (2003) IMF]. We note that such a galaxy-type-dependent estimation of stellar mass will have a much larger impact at the group scale, the focus of the work by Giodini et al. (2009) and Leauthaud et al. (2012), in comparison to the massive clusters we consider here.

As noted earlier, we do not account for the presence of ICL while computing $M^{\rm star}_{500}$. Of the studies shown in Fig. 10, only the work of Gonzalez et al. (2007) measured and included the ICL component, which was found to be approximately 30 per cent of the total light across a sample of $z \approx 0.1$ clusters. Recent studies suggest that the ICL makes up a smaller fraction of the total cluster light at high redshift (≈4 per cent at $z = 0.8$; Burke et al. 2012).

Despite the limitations of the analysis in this work, the stellar fractions we find are nevertheless in reasonable agreement with the results of numerical simulations by Battaglia et al. (2012). These cosmological simulations include sub-grid models for radiative cooling, star formation and AGN feedback (Battaglia et al. 2010). As can be seen in Fig. 10, our observations (in common with the other observational results plotted) show a larger scatter than the simulations, which suggests that the sub-grid models in the simulations need to be improved to capture the larger observed variations in $f^{\rm star}_{500}$ (M_{500}).

The stellar component of clusters makes only a small contribution to the total baryonic mass. Measurements of gas mass within R_{500} ($M^{\rm gas}_{500}$) are available from the literature for five of the objects in the ACT sample (Andersson et al. 2011; Menanteau et al. 2012). In Fig. 10, we plot the total baryon fractions ($f^{\rm b}_{500} = [M^{\rm star}_{500} + M^{\rm gas}_{500}]/M_{500}$) for these clusters, in comparison to the cosmic mean as measured by *WMAP* (Komatsu et al. 2011). We see no evidence for a shortfall of baryons in these objects given current uncertainties, although this is clearly dependent upon the validity of the assumptions made in estimating $f^{\rm star}_{500}$.

7 CONCLUSIONS

We have performed the first study of the stellar mass component of galaxy clusters selected via the SZ effect, using *Spitzer Space Telescope* IR observations of a sample detected by the ACT. We found the following.

(i) The 3.6 and 4.5 μmLFs are similar to those measured for IR-selected cluster samples. We measure both a characteristic magnitude (m^*) and a faint-end slope (α) for the low-redshift ($0.2 < z < 0.5$) ACT sample similar to those found by Mancone et al. (2010), while for the higher redshift sample ($0.5 < z < 1.1$), the ACT clusters have slightly brighter m^* (at the 2σ level).

(ii) The relation between BCG stellar mass and cluster dynamical mass for the ACT sample is shallow ($M_{500} \propto M_*^{0.7\pm0.4}$). The relation is not very well constrained, most likely due to the small sample size. There is strong evidence for the correlation of BCG stellar mass with SZ observables, although again the constraints we obtained on the slopes of these relations are poor. For the scaling with Y_{500}, we found $E(z)^{-2/3}\, D_A^2\, Y_{500} \propto M_*^{1.2\pm0.6}$, with an intrinsic scatter $\sigma_{\log Y_{500}} = 0.25 \pm 0.08$.

(iii) Excluding the cluster J0237−4939, which has anomalously low total stellar mass ($M^{\rm star}_{500}$) compared to its dynamical mass,

we found $M_{500} \propto M_{500}^{\rm star\ 0.9\pm0.4}$, with an intrinsic scatter $\sigma_{\log M_{500}} = 0.10 \pm 0.06$. We also made the first measurement of the scaling of $M_{500}^{\rm star}$ with SZ signal, finding $E(z)^{-2/3}\, D_A^2\, Y_{500} \propto M_{500}^{\rm star\ 1.0\pm0.6}$.

(iv) The stellar fractions that we measured cover the range 0.006–0.034, with median 0.022. These are larger than found in some other studies of clusters of similar mass, but in reasonable agreement with the results of a similar analysis of X-ray-selected clusters using *WISE* data (Lin et al. 2012). For the five clusters with additional gas mass measurements available in the literature, we see no evidence for a shortfall of baryons in clusters relative to the cosmic mean value.

In the future, we intend to extend this study to include ACT clusters on the celestial equator (Hasselfield et al. 2013; Menanteau et al. 2013), where the overlap with deep Sloan Digital Sky Survey Stripe 82 optical photometry (Annis et al. 2011) will allow us to perform a more detailed analysis, without the need for some of the assumptions used in this work.

ACKNOWLEDGEMENTS

This work is based in part on observations made with the *Spitzer Space Telescope*, which is operated by the Jet Propulsion Laboratory, California Institute of Technology under a contract with NASA. MH acknowledges financial support from the Leverhulme trust. This work was supported by the US National Science Foundation through awards AST-0408698 and AST-0965625 for the ACT project, as well as awards PHY-0855887 and PHY-1214379, along with award AST-0955810 to AJB. Funding was also provided by Princeton University, the University of Pennsylvania and a Canada Foundation for Innovation (CFI) award to UBC. ACT operates in the Parque Astronómico Atacama in northern Chile under the auspices of the Comisión Nacional de Investigación Científica y Tecnológica (CONICYT). Computations were performed on the GPC supercomputer at the SciNet HPC Consortium. SciNet is funded by the CFI under the auspices of Compute Canada, the Government of Ontario, the Ontario Research Fund – Research Excellence and the University of Toronto.

REFERENCES

Allen S. W., Rapetti D. A., Schmidt R. W., Ebeling H., Morris R. G., Fabian A. C., 2008, MNRAS, 383, 879
Andersson K. et al., 2011, ApJ, 738, 48
Andreon S., 2010, MNRAS, 407, 263
Annis J. et al., 2011, ApJ, preprint (arXiv:1111.6619)
Aragon-Salamanca A., Baugh C. M., Kauffmann G., 1998, MNRAS, 297, 427
Arnaud M., Evrard A. E., 1999, MNRAS, 305, 631
Arnaud M., Pratt G. W., Piffaretti R., Böhringer H., Croston J. H., Pointecouteau E., 2010, A&A, 517, A92
Arnouts S. et al., 2007, A&A, 476, 137
Balogh M. L., Mazzotta P., Bower R. G., Eke V., Bourdin H., Lu T., Theuns T., 2011, MNRAS, 412, 947
Barmby P., Huang J., Ashby M. L. N., Eisenhardt P. R. M., Fazio G. G., Willner S. P., Wright E. L., 2008, ApJS, 177, 431
Battaglia N., Bond J. R., Pfrommer C., Sievers J. L., 2012, ApJ, preprint (arXiv:1209.4082)
Battaglia N., Bond J. R., Pfrommer C., Sievers J. L., Sijacki D., 2010, ApJ, 725, 91
Bertin E., Arnouts S., 1996, A&AS, 117, 393
Bîrzan L., Rafferty D. A., McNamara B. R., Wise M. W., Nulsen P. E. J., 2004, ApJ, 607, 800
Blanton E. L., Randall S. W., Clarke T. E., Sarazin C. L., McNamara B. R., Douglass E. M., McDonald M., 2011, ApJ, 737, 99
Blanton M. R. et al., 2003, ApJ, 592, 819
Bode P., Ostriker J. P., Vikhlinin A., 2009, ApJ, 700, 989
Bower R. G., Benson A. J., Malbon R., Helly J. C., Frenk C. S., Baugh C. M., Cole S., Lacey C. G., 2006, MNRAS, 370, 645
Bower R. G., McCarthy I. G., Benson A. J., 2008, MNRAS, 390, 1399
Brough S., Collins C. A., Burke D. J., Mann R. G., Lynam P. D., 2002, MNRAS, 329, L53
Brough S., Couch W. J., Collins C. A., Jarrett T., Burke D. J., Mann R. G., 2008, MNRAS, 385, L103
Bruzual G., Charlot S., 2003, MNRAS, 344, 1000 (BC03)
Burke C., Collins C. A., Stott J. P., Hilton M., 2012, MNRAS, 425, 2058
Burke D. J., Collins C. A., Mann R. G., 2000, ApJ, 532, L105
Capozzi D., Collins C. A., Stott J. P., Hilton M., 2012, MNRAS, 419, 2821
Cappellari M. et al., 2006, MNRAS, 366, 1126
Cappellari M. et al., 2012, Nat, 484, 485
Carlstrom J. E., Holder G. P., Reese E. D., 2002, ARA&A, 40, 643
Chabrier G., 2003, PASP, 115, 763
Colless M., 1989, MNRAS, 237, 799
Collins C. A. et al., 2009, Nat, 458, 603
Conroy C., Gunn J. E., White M., 2009, ApJ, 699, 486
Croton D. J. et al., 2005, MNRAS, 356, 1155
De Lucia G., Blaizot J., 2007, MNRAS, 375, 2
De Lucia G., Gabriella S. V., White S. D. M., Croton D., Kauffmann G., 2006, MNRAS, 366, 499
De Propris R., Stanford S. A., Eisenhardt P. R., Dickinson M., Elston R., 1999, AJ, 118, 719
De Propris R. et al., 2003, MNRAS, 342, 725
De Propris R., Stanford S. A., Eisenhardt P. R., Holden B. P., Rosati P., 2007, AJ, 133, 2209
Dressler A., Shectman S. A., 1988, AJ, 95, 985
Duffy A. R., Schaye J., Kay S. T., Dalla Vecchia C., 2008, MNRAS, 390, L64
Dünner R. et al., 2013, ApJ, 762, 10
Ebeling H., Barrett E., Donovan D., Ma C.-J., Edge A. C., van Speybroeck L., 2007, ApJ, 661, L33
Ebeling H., Edge A. C., Allen S. W., Crawford C. S., Fabian A. C., Huchra J. P., 2000, MNRAS, 318, 333
Ebeling H., Edge A. C., Henry J. P., 2001, ApJ, 553, 668
Ebeling H., Edge A. C., Mantz A., Barrett E., Henry J. P., Ma C. J., van Speybroeck L., 2010, MNRAS, 407, 83
Ebeling H., Voges W., Bohringer H., Edge A. C., Huchra J. P., Briel U. G., 1996, MNRAS, 281, 799
Giodini S. et al., 2009, ApJ, 703, 982
Gonzalez A. H., Zaritsky D., Zabludoff A. I., 2007, ApJ, 666, 147
Haarsma D. B. et al., 2010, ApJ, 713, 1037
Hajian A. et al., 2011, ApJ, 740, 86
Hasselfield M. et al., 2013, J. Cosmol. Astropart. Phys., 7, 8
Hilton M. et al., 2009, ApJ, 697, 436
Kelly B. C., 2007, ApJ, 665, 1489
Komatsu E. et al., 2011, ApJS, 192, 18
Kroupa P., 2001, MNRAS, 322, 231
Laidler V. G. et al., 2007, PASP, 119, 1325
Leauthaud A. et al., 2012, ApJ, 746, 95
Lidman C. et al., 2012, MNRAS, 427, 550
Lin Y.-T., Mohr J. J., 2004, ApJ, 617, 879
Lin Y.-T., Mohr J. J., Gonzalez A. H., Stanford S. A., 2006, ApJ, 650, L99
Lin Y.-T., Mohr J. J., Stanford S. A., 2003, ApJ, 591, 749
Lin Y.-T., Mohr J. J., Stanford S. A., 2004, ApJ, 610, 745
Lin Y.-T., Ostriker J. P., Miller C. J., 2010, ApJ, 715, 1486
Lin Y.-T., Stanford S. A., Eisenhardt P. R. M., Vikhlinin A., Maughan B. J., Kravtsov A., 2012, ApJ, 745, L3
Loh Y.-S., Strauss M. A., 2006, MNRAS, 366, 373
Loveday J. et al., 2012, MNRAS, 420, 1239
Makovoz D., Khan I., 2005, in Shopbell P., Britton M., Ebert R., eds, ASP Conf. Ser. 347, Astronomical Data Analysis Software and Systems XIV. Astron. Soc. Pac., San Francisco, p. 81

Mancone C. L., Gonzalez A. H., Brodwin M., Stanford S. A., Eisenhardt P. R. M., Stern D., Jones C., 2010, ApJ, 720, 284
Maraston C., 2005, MNRAS, 362, 799
Markevitch M., 1998, ApJ, 504, 27
Marriage T. A. et al., 2011, ApJ, 737, 61
McNamara B. R., Nulsen P. E. J., Wise M. W., Rafferty D. A., Carilli C., Sarazin C. L., Blanton E. L., 2005, Nat, 433, 45
Mei S. et al., 2009, ApJ, 690, 42
Menanteau F. et al., 2010, ApJ, 723, 1523
Menanteau F. et al., 2012, ApJ, 748, 7
Menanteau F. et al., 2013, ApJ, 765, 67
Mittal R., Hudson D. S., Reiprich T. H., Clarke T., 2009, A&A, 501, 835
Muzzin A., Wilson G., Lacy M., Yee H. K. C., Stanford S. A., 2008, ApJ, 686, 966
Navarro J. F., Frenk C. S., White S. D. M., 1997, ApJ, 490, 493
Oke J. B., 1974, ApJS, 27, 21
Popesso P., Biviano A., Böhringer H., Romaniello M., 2006, A&A, 445, 29
Popesso P., Biviano A., Böhringer H., Romaniello M., 2007, A&A, 464, 451
Pratt G. W., Croston J. H., Arnaud M., Böhringer H., 2009, A&A, 498, 361
Salpeter E. E., 1955, ApJ, 121, 161
Sandage A., 1972, ApJ, 178, 1
Schechter P., 1976, ApJ, 203, 297
Scoville N. et al., 2007, ApJS, 172, 1
Sehgal N. et al., 2011, ApJ, 732, 44
Sifón C. et al., 2013, ApJ, 772, 25
Stott J. P., Edge A. C., Smith G. P., Swinbank A. M., Ebeling H., 2008, MNRAS, 384, 1502
Stott J. P. et al., 2010, ApJ, 718, 23
Strazzullo V. et al., 2010, A&A, 524, A17
Sunyaev R. A., Zeldovich Y. B., 1972, Comments Astrophys. Space Phys., 4, 173
Swetz D. S. et al., 2011, ApJS, 194, 41
Tremaine S. D., Richstone D. O., 1977, ApJ, 212, 311
van Dokkum P. G., Conroy C., 2010, Nat, 468, 940
Vikhlinin A. et al., 2009, ApJ, 692, 1033
Voges W. et al., 1999, A&A, 349, 389
Whiley I. M. et al., 2008, MNRAS, 387, 1253
Wright E. L. et al., 2010, AJ, 140, 1868
Yang X., Mo H. J., van den Bosch F. C., 2008, ApJ, 676, 248

This paper has been typeset from a TEX/LATEX file prepared by the author.